



INSTITUT NATIONAL DE RECHERCHE EN INFORMATIQUE ET EN AUTOMATIQUE

*Modeling fractures as interfaces with nonmatching
grids*

Najla Frih — Vincent Martin — Jean Roberts — Ali Saâda

N° 7517

Janvier 2010

Observation and Modeling for Environmental Sciences

A large, light blue stylized 'R' logo is positioned to the left of the text 'Rapport de recherche'. A horizontal grey brushstroke underline is located below the text.

*Rapport
de recherche*

Modeling fractures as interfaces with nonmatching grids

Najla Frih* , Vincent Martin^{†‡} , Jean Roberts[§] , Ali Saâda*

Theme : Observation and Modeling for Environmental Sciences
Computational Sciences for Biology, Medicine and the Environment
Équipes-Projets Estime et Reo

Rapport de recherche n° 7517 — Janvier 2010 — 26 pages

Abstract: We consider a model for fluid flow in a porous medium with a fracture. In this model, the fracture is represented as an interface between subdomains, where specific equations have to be solved. In this article we analyse the discrete problem, assuming that the fracture mesh and the subdomain meshes are completely independent, but that the geometry of the fracture is respected. We show that despite this non-conformity, first order convergence is preserved with the lowest order Raviart-Thomas(-Nedelec) mixed finite elements. Numerical simulations confirm this result.

Key-words: fractures, barriers, mixed finite elements, flow in porous media, non matching grids, non conforming meshes

* ENIT-LAMSIN, BP 37, 1002 Tunis-le Belvédère, Tunisia. ali.saada@ipein.rnu.tn and najla.frih@lamsin.rnu.tn

† LMAC, UTC, Royallieu, BP 20 529, 60 205 COMPIEGNE Cedex. vincent.martin@utc.fr

‡ Reo Team, INRIA-Paris Rocquencourt, BP 105, 78153 Le Chesnay Cedex.

§ Estime Team, INRIA-Paris Rocquencourt, BP 105, 78153 Le Chesnay Cedex. jean.roberts@inria.fr

Modélisation de fractures comme des interfaces avec des maillages non-conformes

Résumé : Nous étudions un modèle d'écoulement dans milieu poreux contenant une fracture. Dans ce modèle, la fracture est représentée comme une interface entre sous-domaines, au sein de laquelle des équations spécifiques doivent être résolues. Dans le présent article, nous analysons le problème discret, en faisant l'hypothèse que le maillage de la fracture et les maillages des sous-domaines sont complètement indépendants, mais respectent toutefois la géométrie de la fracture. Nous montrons que malgré cette non-conformité, le premier ordre de convergence est conservé pour les éléments finis mixtes de Raviart-Thomas(-Nedelec) de plus bas degré. Des simulations numériques confirment ce résultat.

Mots-clés : fractures, barrières, éléments finis mixtes, écoulement en milieu poreux, maillages non-conformes

1 Introduction

In [2, 1] and in [13] models for flow in fractured porous media were introduced. These were models in which the fractures were treated individually and they were identified as $(n - 1)$ -dimensional interfaces in the n -dimensional domain. These models were analyzed and numerical results obtained with mixed finite element discretization were given. The models were presented as domain decomposition techniques with nonlocal interface conditions on the interface between the subdomains; however, it was assumed that a finite element grid for the entire domain was used and that the fracture coincided with a union of faces of elements of the discretization grid. In [9, 10, 12] this model was extended to a model in which the flow in the fracture was governed by Forchheimer's law while that in the rest of the domain was governed by Darcy's law, and in [10] it was observed that the results were still correct if completely independent grids were used for the subdomains on either side of a fracture and for the fracture itself. The object of this short article is to give a demonstration of the existence and uniqueness of the solution when nonmatching grids are used for the model of [13], which generalizes the model of [2, 1] to include the case of fractures of low permeability, and to show that optimal order convergence is maintained when the Raviart-Thomas-Nedelec elements of lowest order are used. It is interesting to point out that, contrary to what is obtained for the mortar method [5, 6], no restrictions on the mesh size of the interface are necessary to obtain optimal convergence: in particular, one can use a mesh that is very fine in the fracture. We also carry out a numerical study to corroborate these theoretical results.

We remark that in this article we have restricted our attention to the simplest model in which a domain is divided into two disjoint subdomains by a simple fracture and Darcy flow is considered throughout the domain and fracture. However similar fracture models for more complex situations have been studied; e.g. a simple network of fractures cf. [3], Forchheimer flow in the fractures [10, 12], embedded fractures [4, 14], multiphase flow [15], and for the models of [3] and [9, 10, 12], good numerical results have been obtained with nonmatching grids.

We also remark that although we use nonmatching meshes in the subdomains and in the fracture, we do require that the geometry of the fracture is respected by the meshes. In [8], a formulation based on enriched finite elements allows the meshing of the entire domain independently of the fracture, for a case in which there is no flow along the fracture.

2 Description of the problem

Suppose that Ω is a convex domain in \mathbb{R}^n , $n = 2$ or 3 , and denote by $\Gamma = \partial\Omega$ the boundary of Ω . We consider single phase, incompressible flow in Ω and for simplicity we neglect gravitational effects. We suppose that the flow in Ω is governed by the conservation equation together with Darcy's law relating the gradient of the pressure p to the Darcy velocity \mathbf{u} :

$$\begin{aligned} \operatorname{div} \mathbf{u} &= g && \text{in } \Omega \\ \mathbf{u} &= -\mathbf{K}\nabla p && \text{in } \Omega \\ p &= \bar{p} && \text{on } \Gamma, \end{aligned} \tag{1}$$

where p is the pressure, \mathbf{u} the Darcy velocity, \mathbf{K} the hydraulic conductivity (or permeability) tensor, f a source term and \bar{p} the given pressure on the boundary Γ . We suppose that \mathbf{K} is symmetric, bounded, and uniformly positive definite.

For simplicity, for the model problem considered here, it is supposed that the fracture, Ω_f , is a sub-domain of Ω , that there is a hyperplane γ and a unit vector $\mathbf{n} = \mathbf{n}_1 = -\mathbf{n}_2$ normal to γ such that

$$\begin{aligned} \Omega_f &= \left\{ \mathbf{x} = \mathbf{s} + \sigma \mathbf{n} \in \Omega : \mathbf{s} \in \gamma, \right. \\ &\quad \left. \text{and } \sigma \in \left(-\frac{d(\mathbf{s})}{2}, \frac{d(\mathbf{s})}{2}\right) \right\}, \end{aligned}$$

where $d(\mathbf{s})$ denotes the thickness of the fracture at $\mathbf{s} \in \gamma$. It is supposed also that the width function d on γ is bounded above and below by positive constants.

It is further assumed that Ω_f separates Ω into two connected subdomains:

$$\Omega \setminus \overline{\Omega_f} = \Omega_1 \cup \Omega_2, \quad \Omega_1 \cap \Omega_2 = \emptyset.$$

Let $\Gamma_i = \partial\Omega_i \cap \Gamma$ be the part of the boundary of Ω_i in common with the boundary of Ω , $i = 1, 2, f$, and let $\gamma_i = \partial\Omega_i \cap \partial\Omega_f \cap \Omega$ be the part of the boundary of Ω_i in common with the boundary of the fracture Ω_f , $i = 1, 2$. Let \mathbf{n}_i be the outward unit normal vector field on Ω_i , $i = 1, 2, f$.

If we denote by p_i , \mathbf{u}_i , \mathbf{K}_i , and g_i the restrictions of p , \mathbf{u} , \mathbf{K} , and g respectively to Ω_i , $i = 1, 2, f$, and by \bar{p}_i the restriction of \bar{p} to Γ_i , $i = 1, 2, f$, then problem (1) is clearly equivalent to the following transmission problem:

$$\begin{aligned} \operatorname{div} \mathbf{u}_i &= g_i && \text{in } \Omega_i, \quad i = 1, 2, f, \\ \mathbf{u}_i &= -\mathbf{K}_i \nabla p_i && \text{in } \Omega_i, \quad i = 1, 2, f, \\ p_i &= \bar{p}_i && \text{on } \Gamma_i, \quad i = 1, 2, f, \\ p_i &= p_f && \text{on } \gamma_i, \quad i = 1, 2, \\ \mathbf{u}_i \cdot \mathbf{n} &= \mathbf{u}_f \cdot \mathbf{n} && \text{on } \gamma_i, \quad i = 1, 2. \end{aligned} \quad (2)$$

The model problem with the fracture reduced to the interface γ is obtained by averaging across the fracture the first three equations of (2) for the index f . Using the notation ∇_τ (respectively div_τ) for the tangential gradient (respectively the tangential divergence) operator along the fracture γ and denoting by p_γ and \mathbf{u}_γ the pressure and the (tangential) velocity on the fracture interface γ , we obtain the following interface problem:

$$\begin{aligned} \mathbf{u}_i &= -\mathbf{K}_i \nabla p_i && \text{in } \Omega_i \\ \operatorname{div} \mathbf{u}_i &= g_i && \text{in } \Omega_i \\ \mathbf{u}_\gamma &= -\mathbf{K}_\gamma \nabla_\tau p_\gamma && \text{in } \gamma \\ \operatorname{div}_\tau \mathbf{u}_\gamma &= g_\gamma + (\mathbf{u}_1 \cdot \mathbf{n}_1|_\gamma + \mathbf{u}_2 \cdot \mathbf{n}_2|_\gamma) && \text{in } \gamma \\ \kappa_\gamma (p_i - p_\gamma) &= \xi \mathbf{u}_i \cdot \mathbf{n}_i - \bar{\xi} \mathbf{u}_{i+1} \cdot \mathbf{n}_{i+1} && \text{in } \gamma \\ p_i &= \bar{p}_i && \text{on } \Gamma_i \\ p_\gamma &= \bar{p}_\gamma && \text{on } \partial\gamma, \end{aligned} \quad (3)$$

where we have supposed that the index $i = 1, 2$ belongs to $Z_2 = Z/[2]$ so that $2+1=1$, and we have assumed that \mathbf{K}_f is composed of a tangential part $\mathbf{K}_{f,\tau}$ and a normal part $\mathbf{K}_{f,\nu}$ and where $\mathbf{K}_\gamma = \mathbf{K}_{f,\tau} d$ is the tangential permeability $\mathbf{K}_{f,\tau}$ times the width d , $\kappa_\gamma = 2\mathbf{K}_{f,\nu}/d$ is the the normal permeability $\mathbf{K}_{f,\nu}$ divided by half the fracture width, \bar{p}_γ is the average across the fracture of \bar{p}_f , and g_γ is the integral across the fracture of the source term g_f , ξ is a parameter

with $\xi > \frac{1}{2}$ and $\bar{\xi} = 1 - \xi$. The new unknown functions p_γ and \mathbf{u}_γ represent the average pressure across the fracture and the total flux of \mathbf{u}_f across a cross section of the fracture Ω_f . The fifth equation of (3) is derived by averaging the normal component in Darcy's law across the fracture and using a quadrature rule with weights ξ and $\bar{\xi}$ in the quadrature rule for integrating $\mathbf{u}_f \cdot \mathbf{n}$ across the fracture: see [13].

3 Weak formulation of the model problem

The weak formulation of (3) is defined with the Hilbert spaces M and \mathbf{W} :

$$\begin{aligned} M &= L^2(\Omega_1) \times L^2(\Omega_2) \times L^2(\gamma) \\ \mathbf{W} &= \{ \mathbf{v} = (\mathbf{v}_1, \mathbf{v}_2, \mathbf{v}_\gamma) \in H(\text{div}, \Omega_1) \times \\ &\quad H(\text{div}, \Omega_2) \times H(\text{div}_\tau, \gamma), \\ &\quad \text{with } \mathbf{v}_i \cdot \mathbf{n} \in L^2(\gamma), i = 1, 2 \}, \end{aligned}$$

which are equipped with the norms, for an $r = (r_1, r_2, r_\gamma) \in M$ and a $\mathbf{v} = (\mathbf{v}_1, \mathbf{v}_2, \mathbf{v}_\gamma) \in \mathbf{W}$,

$$\begin{aligned} \|r\|_M^2 &= \sum_{i=1}^2 \|r_i\|_{0, \Omega_i}^2 + \|r_\gamma\|_{0, \gamma}^2, \\ \|\mathbf{v}\|_{\mathbf{W}}^2 &= \sum_{i=1}^2 (\|\mathbf{v}_i\|_{0, \Omega_i}^2 + \|\text{div } \mathbf{v}_i\|_{0, \Omega_i}^2) + \|\mathbf{v}_\gamma\|_{0, \gamma}^2 \\ &\quad + \|\text{div}_\tau \mathbf{v}_\gamma\|_{0, \gamma}^2 + \sum_{i=1}^2 \|\mathbf{v}_i \cdot \mathbf{n}\|_{0, \gamma}^2. \end{aligned}$$

Let the bilinear forms $a : \mathbf{W} \times \mathbf{W} \rightarrow \mathbb{R}$ and $b : \mathbf{W} \times M \rightarrow \mathbb{R}$ be defined by

$$\begin{aligned} a(\mathbf{u}, \mathbf{v}) &= \sum_{i=1}^2 (\mathbf{K}_i^{-1} \mathbf{u}_i, \mathbf{v}_i)_{\Omega_i} + (\mathbf{K}_\gamma^{-1} \mathbf{u}_\gamma, \mathbf{v}_\gamma)_\gamma \\ &\quad + \sum_{i=1}^2 (\kappa_\gamma^{-1} (\xi \mathbf{u}_i \cdot \mathbf{n} + \bar{\xi} \mathbf{u}_{i+1} \cdot \mathbf{n}), \mathbf{v}_i \cdot \mathbf{n})_\gamma \\ b(\mathbf{u}, r) &= \sum_{i=1}^2 (\text{div } \mathbf{u}_i, r_i)_{\Omega_i} + (\text{div}_\tau \mathbf{u}_\gamma, r_\gamma)_\gamma \\ &\quad - ([\mathbf{u} \cdot \mathbf{n}], r_\gamma)_\gamma, \end{aligned}$$

where we have used the notation

$$[\mathbf{u} \cdot \mathbf{n}] = \mathbf{u}_1 \cdot \mathbf{n} - \mathbf{u}_2 \cdot \mathbf{n} = \mathbf{u}_1 \cdot \mathbf{n}_1 + \mathbf{u}_2 \cdot \mathbf{n}_2 \quad \text{on } \gamma,$$

and let the linear forms $L_q : M \rightarrow \mathbb{R}$ and $L_d : \mathbf{W} \rightarrow \mathbb{R}$ be those associated with the source term and with the Dirichlet data, respectively:

$$\begin{aligned} L_q(r) &= \sum_{i=1}^2 (q_i, r_i)_{\Omega_i} + (q_\gamma, r_\gamma)_\gamma, \\ L_d(\mathbf{v}) &= - \sum_{i=1}^2 (\mathbf{v}_i \cdot \mathbf{n}_i, \bar{p}_i)_{\Gamma_i} - (\mathbf{v}_\gamma \cdot \mathbf{n}_\gamma, \bar{p}_\gamma)_{\partial\gamma}. \end{aligned}$$

With these spaces and forms the weak form of (3) may be written as

$$\begin{aligned}
 & \mathbf{u} \in \mathbf{W}, p \in M \\
 (\mathcal{P}) \quad & \begin{aligned}
 a(\mathbf{u}, \mathbf{v}) - b(\mathbf{v}, p) &= L_d(\mathbf{v}) & \forall \mathbf{v} \in \mathbf{W} \\
 b(\mathbf{u}, r) &= L_q(r) & \forall r \in M.
 \end{aligned}
 \end{aligned} \tag{4}$$

That (4) has a unique solution is shown in [13].

For convenience of notation we also define the spaces H , \mathbf{H} and \mathbf{M} as follows:

$$\begin{aligned}
 H &= H^1(\Omega_1) \times H^1(\Omega_2) \times H^1(\gamma) \subset M \\
 \mathbf{H} &= (H^1(\Omega_1))^n \times (H^1(\Omega_2))^n \times (H^1(\gamma))^{n-1} \subset \mathbf{W} \\
 \mathbf{M} &= (L^2(\Omega_1))^n \times (L^2(\Omega_2))^n \times (L^2(\gamma))^{n-1} \supset \mathbf{W}
 \end{aligned}$$

with their product norms. We clearly have that the inclusions $H \hookrightarrow M$ and $\mathbf{H} \hookrightarrow \mathbf{W} \hookrightarrow \mathbf{M}$ are continuous and dense (since $\|\mathbf{v}_i \cdot \mathbf{n}\|_{0,\gamma} \leq C \|\mathbf{v}_i\|_{1,\Omega_i}$; $i = 1, 2$ for $\mathbf{v} \in \mathbf{H}$). Also to shorten notation we shall write for $\mathbf{v} \in \mathbf{W}$,

$$\begin{aligned}
 \operatorname{div} \mathbf{v} &= (\operatorname{div} \mathbf{v}_1, \operatorname{div} \mathbf{v}_2, \operatorname{div}_\tau \mathbf{v}_\gamma) \quad \text{and} \\
 \operatorname{Div} \mathbf{v} &= (\operatorname{div} \mathbf{v}_1, \operatorname{div} \mathbf{v}_2, \operatorname{div}_\tau \mathbf{v}_\gamma - [\mathbf{v} \cdot \mathbf{n}]).
 \end{aligned}$$

4 Discretization

Let $\mathcal{T}_{h,i}$ be a finite element partition of Ω_i , $i = 1, 2$, made up of n -dimensional simplicial and/or rectangular elements and $\mathcal{T}_{h,\gamma}$ a finite element partition of γ made up of $(n-1)$ -dimensional simplicial and/or rectangular elements with no matching requirements between any of these partitions. The associated approximation spaces are for the scalar variable

$$M_h = M_{h,1} \times M_{h,2} \times M_{h,\gamma},$$

where $M_{h,i}$, $i = 1, 2$, respectively $M_{h,\gamma}$, is the space of piecewise constant functions associated with $\mathcal{T}_{h,i}$, $i = 1, 2$, respectively $\mathcal{T}_{h,\gamma}$; and for the vector variable

$$\mathbf{W}_h = \mathbf{W}_{h,1} \times \mathbf{W}_{h,2} \times \mathbf{W}_{h,\gamma},$$

where $\mathbf{W}_{h,i}$, $i = 1, 2$, respectively $\mathbf{W}_{h,\gamma}$, is the lowest order Raviart-Thomas(-Nedelec) space associated with $\mathcal{T}_{h,i}$, $i = 1, 2$, respectively $\mathcal{T}_{h,\gamma}$. Recall that $\mathbf{W}_{h,i}$, $i = 1, 2$, respectively $\mathbf{W}_{h,\gamma}$, is the set of functions in $H(\operatorname{div}, \Omega_i)$, $i = 1, 2$ respectively $H(\operatorname{div}_\tau, \gamma)$, whose restrictions to n -simplicial elements are of the form $(a_1 + bx_1, \dots, a_n + bx_n)^t$, and whose restrictions to n -rectangular elements are of the form $(a_1 + b_1x_1, \dots, a_n + b_nx_n)^t$.

Thus $\mathbf{W}_h \subset \mathbf{W}$ and $M_h \subset M$, and the discrete mixed problem may be written as

$$\begin{aligned}
 & \mathbf{u}_h \in \mathbf{W}_h, p_h \in M_h \\
 (\mathcal{P}_h) \quad & \begin{aligned}
 a(\mathbf{u}_h, \mathbf{v}_h) - b(\mathbf{v}_h, p_h) &= L_d(\mathbf{v}_h) & \forall \mathbf{v}_h \in \mathbf{W}_h \\
 b(\mathbf{u}_h, r_h) &= L_q(r_h) & \forall r_h \in M_h.
 \end{aligned}
 \end{aligned} \tag{5}$$

4.1 Interpolation estimates

The following projection operators will be needed for the analysis: for $i=1,2$, let $\Pi_{h,i}$ be the Raviart-Thomas projection onto $\mathbf{W}_{h,i}$ satisfying that for any $\mathbf{v}_i \in (H^1(\Omega_i))^n \cap \mathbf{W}_i$,

$$\begin{aligned} (\operatorname{div}(\Pi_{h,i} \mathbf{v}_i - \mathbf{v}_i), r_{h,i})_{\Omega_i} &= 0 \\ \forall r_{h,i} \in M_{h,i}, \\ \langle (\mathbf{v}_i - \Pi_{h,i} \mathbf{v}_i) \cdot \mathbf{n}_i, \mathbf{w}_{h,i} \cdot \mathbf{n}_i \rangle_{\partial\Omega_i} &= 0 \\ \forall \mathbf{w}_{h,i} \in \mathbf{W}_{h,i}, \end{aligned} \quad (6)$$

and let $\pi_{h,i}$ be the L^2 projection onto $M_{h,i}$ satisfying for any $q_i \in L^2(\Omega_i)$

$$(\pi_{h,i} q_i - q_i, r_{h,i})_{\Omega_i} = 0 \quad \forall r_{h,i} \in M_{h,i}. \quad (7)$$

Similarly, let $\Pi_{h,\gamma}$ be the Raviart-Thomas projection onto $\mathbf{W}_{h,\gamma}$ satisfying that for any $\mathbf{v}_\gamma \in (H^1(\gamma))^{n-1} \cap \mathbf{W}_\gamma$,

$$\begin{aligned} (\operatorname{div}_\tau(\Pi_{h,\gamma} \mathbf{v}_\gamma - \mathbf{v}_\gamma), r_{h,\gamma})_\gamma &= 0 \\ \forall r_{h,\gamma} \in M_{h,\gamma}, \\ \langle (\mathbf{v}_\gamma - \Pi_{h,\gamma} \mathbf{v}_\gamma) \cdot \mathbf{n}_\gamma, \mathbf{w}_{h,\gamma} \cdot \mathbf{n}_\gamma \rangle_{\partial\gamma} &= 0 \\ \forall \mathbf{w}_{h,\gamma} \in \mathbf{W}_{h,\gamma}, \end{aligned} \quad (8)$$

and let $\pi_{h,\gamma}$ be the L^2 projection onto $M_{h,\gamma}$ satisfying for any $q_\gamma \in L^2(\gamma)$

$$(\pi_{h,\gamma} q_\gamma - q_\gamma, r_{h,\gamma})_\gamma = 0 \quad \forall r_{h,\gamma} \in M_{h,\gamma}. \quad (9)$$

These projection operators are known to have the following approximation properties: for $q = (q_1, q_2, q_\gamma) \in M$ and $\mathbf{v} = (\mathbf{v}_1, \mathbf{v}_2, \mathbf{v}_\gamma) \in \mathbf{H}$ and for $\rho \in \mathbb{R}$; $0 \leq \rho \leq 1$, and for $i = 1, 2$,

$$\|q_i - \pi_{h,i} q_i\|_{0,\Omega_i} \leq C h^\rho \|q_i\|_{\rho,\Omega_i}, \quad (10)$$

$$\|q_\gamma - \pi_{h,\gamma} q_\gamma\|_{0,\gamma} \leq C h^\rho \|q_\gamma\|_{\rho,\gamma}, \quad (11)$$

$$\|\mathbf{v}_i - \Pi_{h,i} \mathbf{v}_i\|_{0,\Omega_i} \leq C h \|\mathbf{v}_i\|_{1,\Omega_i}, \quad (12)$$

$$\|\mathbf{v}_\gamma - \Pi_{h,\gamma} \mathbf{v}_\gamma\|_{0,\gamma} \leq C h \|\mathbf{v}_\gamma\|_{1,\gamma}, \quad (13)$$

$$\|\operatorname{div}(\mathbf{v}_i - \Pi_{h,i} \mathbf{v}_i)\|_{0,\Omega_i} \leq C h^\rho \|\operatorname{div} \mathbf{v}_i\|_{\rho,\Omega_i}. \quad (14)$$

$$\|\operatorname{div}_\tau(\mathbf{v}_\gamma - \Pi_{h,\gamma} \mathbf{v}_\gamma)\|_{0,\gamma} \leq C h^\rho \|\operatorname{div}_\tau \mathbf{v}_\gamma\|_{\rho,\gamma}, \quad (15)$$

$$\|(\mathbf{v}_i - \Pi_{h,i} \mathbf{v}_i) \cdot \mathbf{n}_i\|_{0,\gamma} \leq C h^\rho \|\mathbf{v}_i \cdot \mathbf{n}_i\|_{\rho,\gamma}, \quad (16)$$

whenever \mathbf{v} and q are regular enough for the right hand side to be defined. (See [16, Theorem 6.3] or [7] for (12) and (13). The other estimates, (10), (11), (14), (15), and (16), are standard estimates for L^2 -projections.) Then defining

$\pi_h : M \rightarrow M_h$, respectively $\Pi_h : \mathbf{H} \rightarrow \mathbf{W}_h$ to be the product of $\pi_{h,1}$ with $\pi_{h,2}$ and $\pi_{h,\gamma}$, respectively $\Pi_{h,1}$ with $\Pi_{h,2}$ and $\Pi_{h,\gamma}$, we clearly have the following estimates: for $q \in H$ and $\mathbf{v} \in \mathbf{H}$

$$\|q - \pi_h q\|_M \leq C h \|q\|_H, \quad (17)$$

$$\|\mathbf{v} - \Pi_h \mathbf{v}\|_{\mathbf{M}} \leq C h \|\mathbf{v}\|_{\mathbf{H}}, \quad (18)$$

$$\|\operatorname{div}(\mathbf{v} - \Pi_h \mathbf{v})\|_M \leq C h \|\operatorname{div} \mathbf{v}\|_H, \quad (19)$$

so that

$$\|\mathbf{v} - \Pi_h \mathbf{v}\|_{\mathbf{W}} \leq C h \left\{ \|\mathbf{v}\|_{\mathbf{H}} + \|\operatorname{div} \mathbf{v}\|_H + \sum_{i=1}^2 \|\mathbf{v}_i \cdot \mathbf{n}\|_{1,\gamma} \right\}, \quad (20)$$

whenever $\operatorname{div} \mathbf{v} \in H$ and $\mathbf{v}_i \cdot \mathbf{n} \in H^1(\gamma)$, $i = 1, 2$. It is also clear that both of these maps are continuous:

$$\begin{aligned} \|\pi_h q\|_M &\leq \|q\|_M, \quad \forall q \in M \\ \|\Pi_h \mathbf{v}\|_{\mathbf{W}} &\leq C \|\mathbf{v}\|_{\mathbf{H}}, \quad \forall \mathbf{v} \in \mathbf{H}, \end{aligned} \quad (21)$$

where the first inequality is well known for L^2 -projections, and the second follows from (12) and (13) and from (14), (15), and (16) with $\rho = 0$. Recalling the definition of $\operatorname{Div} : \mathbf{W} \rightarrow M$ and defining $\operatorname{Div}_h : \mathbf{W}_h \rightarrow M_h$ as

$$\begin{aligned} \operatorname{Div}(\mathbf{v}) &= (\operatorname{div} \mathbf{v}_1, \operatorname{div} \mathbf{v}_2, \operatorname{div}_\tau \mathbf{v}_\gamma - [\mathbf{v} \cdot \mathbf{n}]) \\ \operatorname{Div}_h(\mathbf{v}_h) &= (\operatorname{div} \mathbf{v}_{h,1}, \operatorname{div} \mathbf{v}_{h,2}, \operatorname{div}_\tau \mathbf{v}_{h,\gamma} - \pi_{h,\gamma}[\mathbf{v}_h \cdot \mathbf{n}]), \end{aligned}$$

except for the case of matching grids, we do not have commutativity of the diagram

$$\begin{array}{ccc} \mathbf{H} & \xrightarrow{\operatorname{Div}} & M \\ \downarrow \Pi_h & & \downarrow \pi_h \\ \mathbf{W}_h & \xrightarrow{\operatorname{Div}_h} & M_h \end{array}$$

i.e. in general

$$\operatorname{Div}_h \Pi_h \mathbf{v} \neq \pi_h \operatorname{Div} \mathbf{v},$$

for nonmatching grids, even though we do have

$$\begin{aligned} \operatorname{div} \Pi_{h,i} \mathbf{v}_i &= \pi_{h,i} \operatorname{div} \mathbf{v}_i, \quad \forall \mathbf{v}_i \in (H^1(\Omega_i))^n, \\ &\quad i = 1, 2, \\ \operatorname{div}_\tau \Pi_{h,\gamma} \mathbf{v}_\gamma &= \pi_{h,\gamma} \operatorname{div}_\tau \mathbf{v}_\gamma, \quad \forall \mathbf{v}_\gamma \in (H^1(\gamma))^{n-1}. \end{aligned}$$

This is due to the fact that in general for nonmatching grids

$$\pi_{h,\gamma}(\mathbf{v}_i \cdot \mathbf{n}) \neq \pi_{h,\gamma}(\Pi_{h,i} \mathbf{v}_i \cdot \mathbf{n}) \quad i = 1, 2. \quad (22)$$

This can be seen in particular when the space $M_{h,\gamma}$ is much richer than the space of normal traces on γ of elements of $\mathbf{W}_{h,i}$.

4.2 Approximation estimates

The proof of the existence and uniqueness of the solution of the discrete problem (5) as well as the error estimates will follow from lemmas 1 and 2 given below. All of the demonstrations follow closely those in [13].

Lemma 1 *With the hypotheses made concerning the permeabilities and the fracture width and with the assumption that $\xi > \frac{1}{2}$ the bilinear form $a(\cdot, \cdot)$ is elliptic on the space $\widetilde{\mathbf{W}}_h$,*

$$\widetilde{\mathbf{W}}_h = \{\mathbf{v}_h \in \mathbf{W}_h : b(\mathbf{v}_h, r_h) = 0, \quad \forall r_h \in M_h\},$$

with a constant independent of h : i.e. there exists a constant $C_a > 0$ such that

$$a(\mathbf{v}_h, \mathbf{v}_h) \geq C_a \|\mathbf{v}_h\|_{\widetilde{\mathbf{W}}}^2, \quad \forall \mathbf{v}_h \in \widetilde{\mathbf{W}}_h.$$

Proof: Suppose $\mathbf{v}_h \in \widetilde{\mathbf{W}}_h$, and consider the test function $r_h \in M_h$ in (5) defined by

$$r_h = (\operatorname{div} \mathbf{v}_{h,1}, \operatorname{div} \mathbf{v}_{h,2}, \operatorname{div}_\tau \mathbf{v}_{h,\gamma} - \pi_{h,\gamma}[\mathbf{v}_h \cdot \mathbf{n}]).$$
 Then

$$0 = b(\mathbf{v}_h, r_h) = \sum_{i=1}^2 \|\operatorname{div} \mathbf{v}_{h,i}\|_{0,\Omega_i}^2 + \|\operatorname{div}_\tau \mathbf{v}_{h,\gamma} - \pi_{h,\gamma}[\mathbf{v}_h \cdot \mathbf{n}]\|_{0,\gamma}^2$$

and we have

$$\begin{aligned} \operatorname{div} \mathbf{v}_{h,i} &= 0, \quad i = 1, 2 \\ \operatorname{div}_\tau \mathbf{v}_{h,\gamma} &= \pi_{h,\gamma}[\mathbf{v}_h \cdot \mathbf{n}], \end{aligned}$$

Thus, using (21) it follows that

$$\begin{aligned} \|\mathbf{v}_h\|_{\widetilde{\mathbf{W}}}^2 &\leq \sum_{i=1}^2 \|\mathbf{v}_{h,i}\|_{0,\Omega_i}^2 + \|\mathbf{v}_{h,\gamma}\|_{0,\gamma}^2 \\ &\quad + 3 \sum_{i=1}^2 \|\mathbf{v}_{h,i} \cdot \mathbf{n}\|_{0,\gamma}^2. \end{aligned}$$

Also a can be written as

$$\begin{aligned} a(\mathbf{v}_h, \mathbf{v}_h) &= \sum_{i=1}^2 (\mathbf{K}_i^{-1} \mathbf{v}_{h,i}, \mathbf{v}_{h,i})_{\Omega_i} \\ &\quad + (\mathbf{K}_\gamma^{-1} \mathbf{v}_{h,\gamma}, \mathbf{v}_{h,\gamma})_\gamma \\ &\quad + \xi \sum_{i=1}^2 \left(\frac{\mathbf{v}_{h,i} \cdot \mathbf{n}}{\kappa_\gamma^{1/2}}, \frac{\mathbf{v}_{h,i} \cdot \mathbf{n}}{\kappa_\gamma^{1/2}} \right)_\gamma \\ &\quad + 2 \bar{\xi} \left(\frac{\mathbf{v}_{h,1} \cdot \mathbf{n}}{\kappa_\gamma^{1/2}}, \frac{\mathbf{v}_{h,2} \cdot \mathbf{n}}{\kappa_\gamma^{1/2}} \right)_\gamma. \end{aligned} \tag{23}$$

So, for $\mathbf{v}_h \in \widetilde{\mathbf{W}}_h$,

$$\begin{aligned} a(\mathbf{v}_h, \mathbf{v}_h) &\geq C \left(\sum_{i=1}^2 \|\mathbf{v}_{h,i}\|_{0,\Omega_i}^2 + \|\mathbf{v}_{h,\gamma}\|_{0,\gamma}^2 \right) \\ &\quad + \min\{1, \xi - \bar{\xi}\} \sum_{i=1}^2 \left\| \frac{\mathbf{v}_{h,i} \cdot \mathbf{n}}{\kappa_\gamma^{1/2}} \right\|_{0,\gamma}^2 \\ &\geq C(\mathbf{K}_1, \mathbf{K}_2, \mathbf{K}_\gamma, \kappa_\gamma, \xi) \|\mathbf{v}_h\|_{\widetilde{\mathbf{W}}}^2, \end{aligned}$$

where the constant $C_a = C(\mathbf{K}_1, \mathbf{K}_2, \mathbf{K}_\gamma, \kappa_\gamma, \xi) > 0$ depends on the permeability tensor \mathbf{K} , the width function d on the fracture and the quadrature parameter $\xi > \frac{1}{2}$ but not on the mesh parameter h . \blacksquare

Lemma 2 *The bilinear form $b : \mathbf{W}_h \times M_h$ satisfies the inf-sup condition with a constant independent of h : i.e. there exists a constant $C_b > 0$ such that*

$$\forall r_h \in M_h, \quad \sup_{\mathbf{v}_h \in \mathbf{W}_h} \frac{b(\mathbf{v}_h, r_h)}{\|\mathbf{v}_h\|_{\mathbf{W}}} \geq C_b \|r_h\|_M.$$

Proof: Given $r_h \in M_h$, using auxillary problems we construct an element $\mathbf{v}_h \in \mathbf{W}_h$ such that $b(\mathbf{v}_h, r_h) = \|r_h\|_M^2$ and $\|\mathbf{v}_h\|_{\mathbf{W}} \leq C \|r_h\|_M$, where C depends on the constants of elliptic regularity for the auxillary problems.

For $r_h = (r_{h,1}, r_{h,2}, r_{h,\gamma}) \in M_h$, let $\zeta \in H^2(\Omega)$ be the solution of

$$\begin{aligned} -\Delta \zeta &= \tilde{r}_h & \text{in } \Omega, \\ \zeta &= 0 & \text{on } \partial\Omega, \end{aligned} \quad (24)$$

where $\tilde{r}_h \in L^2(\Omega)$ is given by $\tilde{r}_{h,|\Omega_i} = r_{h,i}$, $i = 1, 2$. Pose $\mathbf{v}_i = -\nabla \zeta|_{\Omega_i}$, $i = 1, 2$, and let $\mathbf{v}_{h,i} = \Pi_{h,i} \mathbf{v}_i$. Then

$$\begin{aligned} \operatorname{div} \mathbf{v}_{h,i} &= \operatorname{div} \Pi_{h,i} \mathbf{v}_i = \pi_{h,i} \operatorname{div} \mathbf{v}_i \\ &= \pi_{h,i} r_{h,i} = r_{h,i}. \end{aligned}$$

Next let $\zeta_\gamma \in H^2(\gamma)$ be the solution of

$$\begin{aligned} -\Delta_\tau \zeta_\gamma &= r_{h,\gamma} + \pi_{h,\gamma} [\mathbf{v}_h \cdot \mathbf{n}] & \text{in } \gamma, \\ \zeta_\gamma &= 0 & \text{on } \partial\gamma, \end{aligned} \quad (25)$$

where we note that even though $[\mathbf{v} \cdot \mathbf{n}] = 0$, in general with non matching grids, $[\mathbf{v}_h \cdot \mathbf{n}] \neq 0$ and $\pi_{h,\gamma} [\mathbf{v}_h \cdot \mathbf{n}] \neq 0$, cf. (22). Pose $\mathbf{v}_\gamma = -\nabla_\tau \zeta_\gamma$, and let $\mathbf{v}_{h,\gamma} = \Pi_{h,\gamma} \mathbf{v}_\gamma$. Then we have

$$\begin{aligned} \operatorname{div}_\tau \mathbf{v}_{h,\gamma} &= \operatorname{div}_\tau \Pi_{h,\gamma} \mathbf{v}_\gamma = \pi_{h,\gamma} \operatorname{div}_\tau \mathbf{v}_\gamma \\ &= r_{h,\gamma} + \pi_{h,\gamma} [\mathbf{v}_h \cdot \mathbf{n}]. \end{aligned}$$

Thus $\mathbf{v}_h = (\mathbf{v}_{h,1}, \mathbf{v}_{h,2}, \mathbf{v}_{h,\gamma}) \in \mathbf{W}_h$ and

$$\begin{aligned} b(\mathbf{v}_h, r_h) &= \sum_{i=1}^2 (r_{h,i}, r_{h,i})_{\Omega_i} \\ &\quad + (r_{h,\gamma} + \pi_{h,\gamma} [\mathbf{v}_h \cdot \mathbf{n}], r_{h,\gamma})_\gamma \\ &\quad - (\pi_{h,\gamma} [\mathbf{v}_h \cdot \mathbf{n}], r_{h,\gamma})_\gamma, \\ &= \|r_h\|_M^2. \end{aligned}$$

To bound $\|\mathbf{v}_h\|_{\mathbf{W}}^2$ in terms of $\|r_h\|_M$, we recall that

$$\begin{aligned} \|\mathbf{v}_h\|_{\mathbf{W}}^2 &= \sum_{i=1}^2 (\|\mathbf{v}_{h,i}\|_{0,\Omega_i}^2 + \|\operatorname{div} \mathbf{v}_{h,i}\|_{0,\Omega_i}^2) \\ &\quad + \|\mathbf{v}_{h,\gamma}\|_{0,\gamma}^2 + \|\operatorname{div}_\tau \mathbf{v}_{h,\gamma}\|_{0,\gamma}^2 \\ &\quad + \sum_{i=1}^2 \|\mathbf{v}_{h,i} \cdot \mathbf{n}\|_{0,\gamma}^2 \end{aligned}$$

and treat the terms separately. For the first term we have

$$\begin{aligned}
 \sum_{i=1}^2 \|\mathbf{v}_{h,i}\|_{0,\Omega_i}^2 &= \sum_{i=1}^2 \|\Pi_{h,i} \mathbf{v}_i\|_{0,\Omega_i}^2 \\
 &\leq C \sum_{i=1}^2 \|\mathbf{v}_i\|_{1,\Omega_i}^2 \\
 &= C \sum_{i=1}^2 \|\nabla \zeta\|_{1,\Omega_i}^2 \\
 &= C \|\nabla \zeta\|_{1,\Omega}^2 \\
 &\leq C \|\zeta\|_{2,\Omega}^2 \\
 &\leq C(\Omega) \|\tilde{r}_h\|_{0,\Omega}^2,
 \end{aligned}$$

and for the second term we have immediately

$$\sum_{i=1}^2 \|\operatorname{div} \mathbf{v}_{h,i}\|_{0,\Omega_i}^2 = \sum_{i=1}^2 \|r_{h,i}\|_{0,\Omega_i}^2.$$

The third term is estimated quite similarly to the first term:

$$\begin{aligned}
 \|\mathbf{v}_{h,\gamma}\|_{0,\gamma}^2 &= \|\Pi_{h,\gamma} \mathbf{v}_\gamma\|_{0,\gamma}^2 \leq C \|\mathbf{v}_\gamma\|_{1,\gamma}^2 \\
 &= C \|\nabla_\tau \zeta_\gamma\|_{1,\gamma}^2 \leq C \|\zeta_\gamma\|_{2,\gamma}^2 \\
 &\leq C(\gamma) \|r_{h,\gamma} + \pi_{h,\gamma} [\mathbf{v}_h \cdot \mathbf{n}]\|_{0,\gamma}^2 \\
 &\leq C \left(\|r_{h,\gamma}\|_{0,\gamma}^2 + \|[\mathbf{v}_h \cdot \mathbf{n}]\|_{0,\gamma}^2 \right) \\
 &\leq C \left(\|r_{h,\gamma}\|_{0,\gamma}^2 + \sum_{i=1}^2 \|(\mathbf{v}_i - \mathbf{v}_{h,i}) \cdot \mathbf{n}\|_{0,\gamma}^2 \right) \\
 &\leq C \left(\|r_{h,\gamma}\|_{0,\gamma}^2 + \sum_{i=1}^2 \|\mathbf{v}_i\|_{1,\Omega_i}^2 \right) \\
 &\leq C \left(\|r_{h,\gamma}\|_{0,\gamma}^2 + \sum_{i=1}^2 \|r_{h,i}\|_{0,\Omega_i}^2 \right),
 \end{aligned}$$

where we have used the fact $[\mathbf{v} \cdot \mathbf{n}] = 0$, the estimate (16) and the continuity of the trace operator. For the fourth term we have

$$\begin{aligned}
 \|\operatorname{div}_\tau \mathbf{v}_{h,\gamma}\|_{0,\gamma}^2 &= \|r_{h,\gamma} + \pi_{h,\gamma} [\mathbf{v}_h \cdot \mathbf{n}]\|_{0,\gamma}^2 \\
 &\leq C \left(\|r_{h,\gamma}\|_{0,\gamma}^2 + \sum_{i=1}^2 \|r_{h,i}\|_{0,\Omega_i}^2 \right).
 \end{aligned}$$

Finally for the last term we obtain

$$\begin{aligned}
 \sum_{i=1}^2 \|\mathbf{v}_{h,i} \cdot \mathbf{n}\|_{0,\gamma}^2 &= \sum_{i=1}^2 \|\Pi_{h,i} \mathbf{v}_i \cdot \mathbf{n}\|_{0,\gamma}^2 \\
 &\leq \sum_{i=1}^2 \|\mathbf{v}_i \cdot \mathbf{n}\|_{0,\gamma}^2 \\
 &\leq C \sum_{i=1}^2 \|\mathbf{v}_i\|_{1,\Omega_i}^2 \\
 &\leq C \sum_{i=1}^2 \|r_{h,i}\|_{0,\Omega_i}^2.
 \end{aligned}$$

Thus the constant $C = C(\Omega_1, \Omega_2, \gamma)$ is independent of h . \blacksquare

Applying Brezzi's theorem [16, Theorem 10.4] and using Lemmas 1 and 2 we obtain the following theorem.

Theorem 1 *If $(\mathbf{u}, p) \in \mathbf{W} \times M$ is the solution of problem (\mathcal{P}) and $(\mathbf{u}_h, p_h) \in \mathbf{W}_h \times M_h$ is the solution of problem (\mathcal{P}_h) , then*

$$\|p - p_h\|_M + \|\mathbf{u} - \mathbf{u}_h\|_{\mathbf{W}} \leq C \left(\inf_{q_h \in M_h} \|p - q_h\|_M + \inf_{\mathbf{v}_h \in \mathbf{W}_h} \|\mathbf{u} - \mathbf{v}_h\|_{\mathbf{W}} \right).$$

Combining Theorem 1 with the interpolation estimates (17) and (20) we obtain

Theorem 2 *If $(\mathbf{u}, p) \in \mathbf{W} \times M$ is the solution of problem (\mathcal{P}) and $(\mathbf{u}_h, p_h) \in \mathbf{W}_h \times M_h$ is the solution of problem (\mathcal{P}_h) , and \mathbf{u} and p are sufficiently regular, then*

$$\|p - p_h\|_M + \|\mathbf{u} - \mathbf{u}_h\|_{\mathbf{W}} \leq Ch \left(\|p\|_H + \|\mathbf{u}\|_{\mathbf{H}} + \|\operatorname{div} \mathbf{u}\|_H + \sum_{i=1}^2 \|\mathbf{v}_i \cdot \mathbf{n}\|_{1,\gamma} \right). \quad (26)$$

Numerical results

In this section, we present some numerical results that confirm the convergence estimate provided in Theorem 2. Three cases are shown to illustrate the very different flow regimes the fracture model can handle: in Section 4.3, the fracture is highly permeable, whereas in Section 4.4 it represents a barrier with a very low permeability. Finally, in Section 4.5 the fracture yields both regimes at two different locations. In all cases, the expected convergence rate in the L^2 norm for the velocity and for the pressure is attained, regardless of the degree of nonconformity of the grid.

As stated earlier, we have assumed that the discretization mesh \mathcal{T}_h respects the fracture, but that the meshes on Ω_1, Ω_2 and γ may be chosen independently. We will say that the mesh $\mathcal{T}_h = (\mathcal{T}_{h_1}, \mathcal{T}_{h_2}, \mathcal{T}_{h_\gamma})$ is made up of three meshes with \mathcal{T}_{h_i} being a mesh on Ω_i , $i = 1, 2$, and \mathcal{T}_{h_γ} being a mesh of γ . In all of the experiments reported here, for $i = 1, 2$, \mathcal{T}_{h_i} has been taken to be a uniform mesh made up of squares of edge-length h_i , and \mathcal{T}_{h_γ} to be a uniform mesh made up of intervals of length h_γ . The mesh parameter h for \mathcal{T}_h is

$$h = \max\{h_1, h_2, h_\gamma\}.$$

In this case to say that the grid is conforming simply means that $h_1 = h_2 = h_\gamma$.

In the experiments that follow, we denote by (p_h, \mathbf{u}_h) the solution of (\mathcal{P}_h) obtained with a *nonconforming* mesh \mathcal{T}_h . In the convergence computations, the parameters determining \mathcal{T}_h were taken as follows: $h_1 = 1/n$, $h_2 = 1/(n+8)$ and $h_\gamma = 1/(10n)$ in the case of finer discretization in the fracture or $h_\gamma = 5/n$ in the case of a coarser discretization in the fracture, for some $n \in [20, 600]$. We point out that to depict the solutions, both pressure and velocity, we have used a rather coarse mesh so that the mesh as well as the arrows representing the velocity may be clearly seen.

In all of the experiments the parameter ξ in the fifth equation of model (3) is taken to be $\xi = 2/3$.

To compute relative L^2 errors for the pressure and Darcy velocity we calculate a *reference solution* p_η^* and velocity \mathbf{u}_η^* which is the solution of (\mathcal{P}_h) obtained with a *conforming* mesh \mathcal{T}_η^* , (i.e. $\eta_1 = \eta_2 = \eta_\gamma = \eta$) with $\eta < h$ whenever h is the mesh parameter in the experiment under consideration. (Here $\eta \approx 1/1200$.)

The L^2 errors are approximated as follows: the “intersection mesh” (coarsest common refinement) $\mathcal{T}_\eta^* \cap \mathcal{T}_h$ is computed (in each subdomain and in γ). Then, the reference $(p_\eta^*, \mathbf{u}_\eta^*)$ and nonconforming (p_h, \mathbf{u}_h) solutions are interpolated on this intersection mesh. The difference is computed, squared and numerically integrated to obtain $\|p_h - p_\eta^*\|_M^2$ and $\|\mathbf{u}_h - \mathbf{u}_\eta^*\|_M^2$. With sufficient regularity, unless h is of the same order as η , these norms should behave as $\mathcal{O}(h)$ according to Theorem 2.

In all test cases the domain is a 2 by 1 rectangle with the fracture interface γ being the central vertical bisector, so that Ω_1 and Ω_2 are the remaining lefthand and righthand squares when γ is removed from the domain. In both test cases the permeability is scalar with $K_1 = K_2 = 1$, the tops and bottoms of the two subdomains are impermeable and there is a unit pressure drop from the righthand side of the domain to the lefthand side of the domain. The permeability K_f in the fracture is also scalar and the width d of the physical fracture is $d = 0.001$.

In the first test case the fracture is highly permeable and there is a pressure drop from the top to the bottom of the fracture so that the fluid flows along the fracture as well as from right to left; see Figure 1. In the second test case the central part of the fracture is a barrier with very low permeability so that the fluid flows from right to left but must flow around the fracture; see Figure 2. In the third test case the fracture is highly permeable at the top and bottom parts and represents a barrier in the central part. There is a pressure drop from the top to the bottom; see Figure 3.

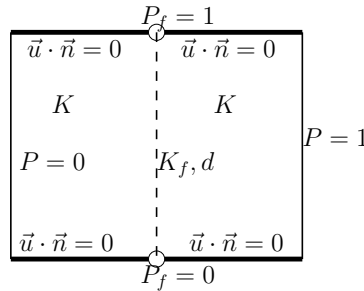


Figure 1: Test-case 1 with a large permeability in the fracture. Homogeneous Neumann boundary conditions are depicted with fat lines. The fracture is depicted with a dashed line.

4.3 First test-case : a highly permeable fracture

In this test-case (see Figure 1), the permeability K_f in the fracture is $K_f = 2000$ and thus $K_\gamma = K_f d = 2$. Dirichlet conditions are imposed on the fracture boundaries: there is a unit pressure drop from the top of the fracture to the bottom. Thus the fluid tends to flow from right to left and also to flow rapidly along the very permeable fracture from top to bottom. There is fluid exchange

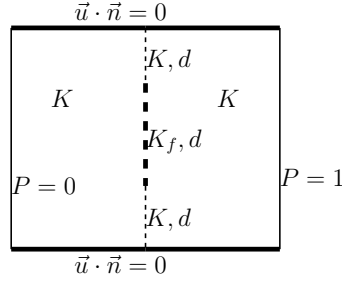


Figure 2: Test-case 2 with a geological barrier. The impervious part of the fracture is limited to the central zone.

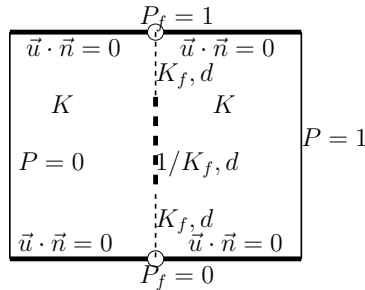


Figure 3: Test-case 3 with with a large permeability zone and a geological barrier. The impervious part of the fracture is limited to the central zone.

between the fracture and the rock matrix as fluid from the fracture enters the rock matrix at the top and fluid from the matrix enters the fracture at the bottom. The normal velocity is discontinuous across the fracture.

A reference computation performed with a conforming mesh is shown in Figure 4, where we recall that the grid is considerably coarsened for visualization purposes.

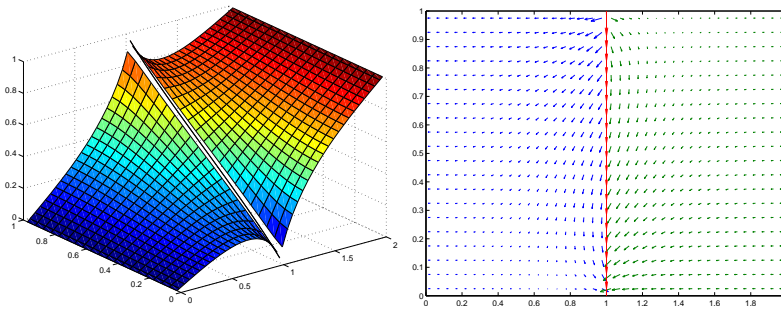


Figure 4: Test case 1. Pressure (left) and Darcy velocity (right) with conforming meshes ($h_1 = h_2 = h_\gamma = 1/20$). $K_f = 2000, d = 0.001$. (The grids are quite coarse for visualization purposes.)

A solution obtained with a nonconforming mesh is shown in Figure 5 in the case of a highly refined fracture mesh, and in Figure 6 in the case of a coarse fracture mesh. When the fracture mesh is coarser than the surrounding mesh, some small oscillations in the pressure and Darcy velocity can be seen in the vicinity of the fracture.

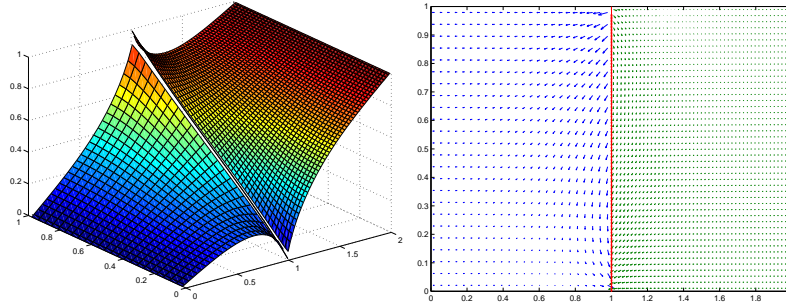


Figure 5: Test case 1. Pressure (left) and Darcy velocity (right) with nonconforming meshes: $h_1 = 1/24, h_\gamma = 1/91, h_2 = 1/47$ (the fracture mesh is **finer** than the other meshes). $K_f = 2000, d = 0.001$.

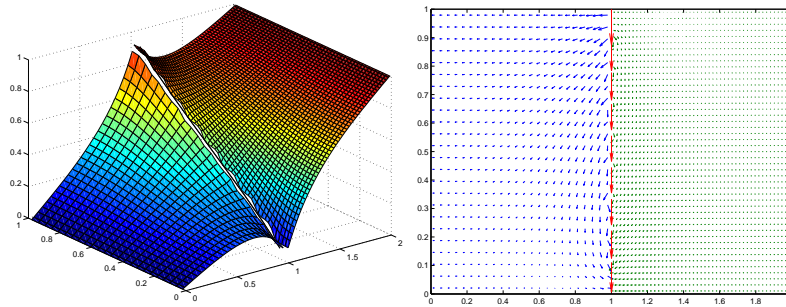


Figure 6: Test case 1. Pressure (left) and Darcy velocity (right) with nonconforming meshes: $h_1 = 1/24, h_\gamma = 1/9, h_2 = 1/47$ (the fracture mesh is **coarser** than the other meshes). $K_f = 2000, d = 0.001$. Small oscillations occur close to the fracture.

The convergence curves for the pressure and for the Darcy velocity in the L^2 norm are shown in Figure 7 for a finely meshed fracture and for a coarsely meshed fracture. For comparison, we also show the convergence curves for conforming meshes, which are almost superimposed with the curves for the finely meshed fracture case. One obtains a linear convergence in both cases for both the pressure and for the Darcy velocity. One can even notice a slightly improved convergence rate for the Darcy velocity in the case of conforming meshes and in the case of a more finely meshed fracture.

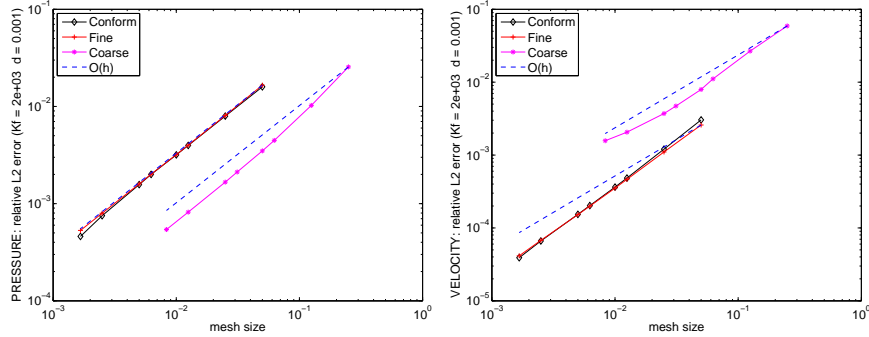


Figure 7: Test case 1. Relative L^2 error variation as a function of the mesh size h . The three meshes are nonconforming at the interface, and the fracture is either **finely** (crosses) or **coarsely** (stars) meshed. $h_1 \approx h_2 \in [1/20, 1/600]$, and $h_\gamma \approx 0.1 h_1$ (finely meshed fracture) or $h_\gamma \approx 5 h_1$ (coarsely meshed fracture). We also report the convergence history in the conforming case (diamonds, $h_1 = h_2 = h_\gamma$). $K_f = 2000, d = 0.001$. **Left:** pressure error. **Right:** velocity error.

4.4 Second test-case: a geological barrier

In the second test-case (see Figure 2) the central half of the fracture is a barrier with $K_f = 0.002$ so that $\kappa_\gamma = 2K_f/d = 4$ while in the upper and lower quarters of the fracture the permeability K_f is the same as in the surrounding rock matrix: $K_f = K_1 = K_2 = 1$. Homogeneous Neumann conditions are imposed at the upper and lower boundaries of the fracture. The fluid tends to avoid the impervious fracture, and the pressure is discontinuous across the fracture. See the solution with conforming meshes in Figure 8.

A solution obtained with a nonconforming mesh is shown in Figure 9 in the case of a refined fracture mesh, and in Figure 10 in the case of a coarse fracture mesh. When the fracture mesh is much finer than the surrounding mesh, some large oscillations in the fracture pressure occur. These spurious oscillations decay when the meshes are refined while keeping the same relation between h_1, h_2 and h_γ ; cf. Figure 11.

In Figure 12, the L^2 norm convergence curves for the pressure and for the Darcy velocity are shown for a discretization with a finely meshed fracture and with a coarsely meshed fracture. As before for comparison, we also show the convergence with conforming meshes, which is very similar to that of the finely mesh case. The convergence rate for the pressure is linear as predicted theoretically. Note however that, in both cases, the convergence of the Darcy velocity is sublinear at first ($\mathcal{O}(h^{1/2})$), before slowly reaching an asymptotic linear behavior. This behavior is also observed for conforming meshes.

We suspect that the $\mathcal{O}(h^{1/2})$ behavior of the velocity is caused by a lack of regularity of the solution at the extremities of the fracture. Indeed, let us consider the Darcy problem posed only in the Ω_2 with the same boundary conditions on the upper, lower and righthand side boundaries as in test case 2 but with, in place of the fracture transmission conditions on the lefthand side, the boundary condition $\mathbf{u} \cdot \mathbf{n} = 0$ for $1/4 \leq y \leq 3/4$ and $p = 0$ for $y < 1/4$ and for $3/4 < y$ cf Figure 13. As the type of boundary condition changes from

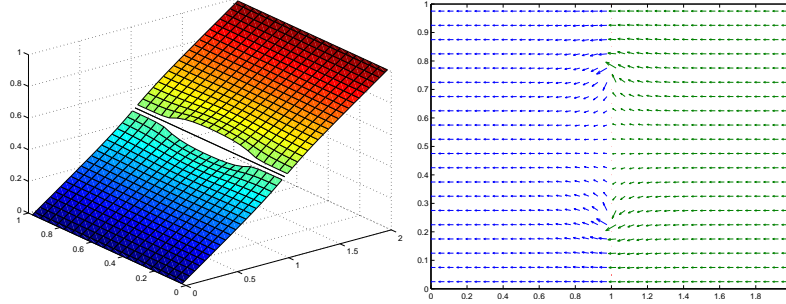


Figure 8: Test case 2. Pressure (left) and Darcy velocity (right) with conforming meshes ($h_1 = h_2 = h_\gamma = 1/20$). $K_f = 0.002$, $d = 0.001$. The very small velocity can hardly be seen in the fracture.

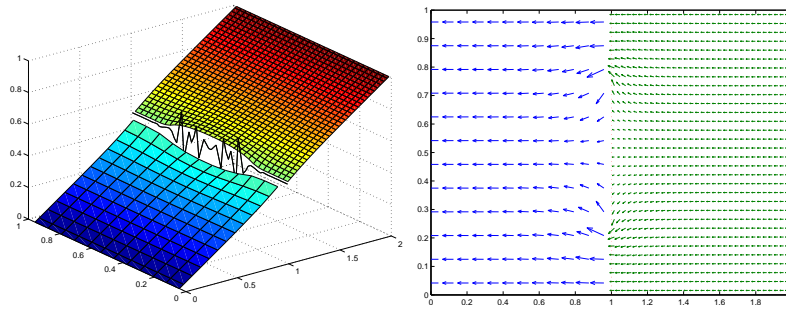


Figure 9: Test case 2. Pressure (left) and Darcy velocity (right) with nonconforming meshes: $h_1 = 1/12$, $h_\gamma = 1/64$, $h_2 = 1/32$ (the fracture mesh is **finer** than the other meshes). $K_f = 0.002$, $d = 0.001$. The fracture pressure has large oscillations.

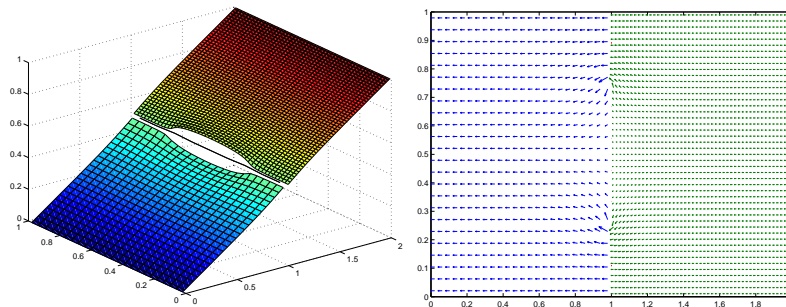


Figure 10: Test case 2. Pressure (left) and Darcy velocity (right) with nonconforming meshes: $h_1 = 1/24$, $h_\gamma = 1/9$, $h_2 = 1/47$ (the fracture mesh is **coarser** than the other meshes). $K_f = 0.002$, $d = 0.001$.

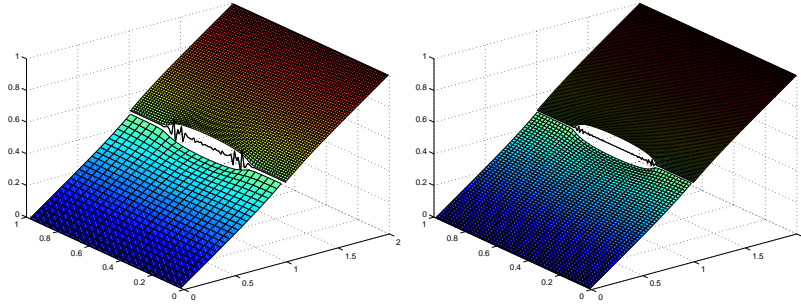


Figure 11: Test case 2. Pressure evolution when h is refined (**fine** fracture case). Left: $h_1 = 1/24, h_\gamma = 1/128, h_2 = 1/64$. Right: $h_1 = 1/48, h_\gamma = 1/256, h_2 = 1/128$. $K_f = 0.002, d = 0.001$. The oscillations decrease with h .

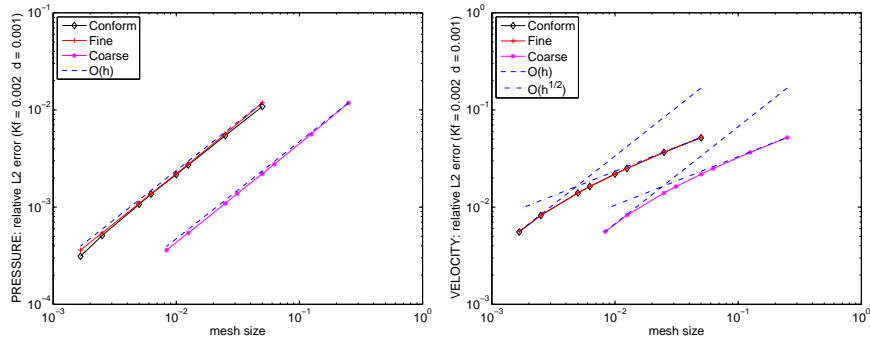


Figure 12: Test case 2. Relative L^2 error as a function of h . The three meshes are nonconforming at the interface and the fracture is either **finely** (crosses) or **coarsely** (stars) meshed. $h_1 \approx h_2 \in [1/20, 1/600]$, and $h_\gamma \approx 0.1 h_1$ (finely meshed fracture) or $h_\gamma \approx 5 h_1$ (coarsely meshed fracture). We also report the convergence history in the conforming case (diamonds, $h_1 = h_2 = h_\gamma$). $K_f = 0.002, d = 0.001$. **Left:** pressure error. **Right:** velocity error.

Neumann to Dirichlet, the solution has locally the same type of singularity as $r^{1/2} \sin(\theta/2)$ and thus belongs to $H^{3/2-\varepsilon}(\Omega)$ for each $\varepsilon > 0$, see [11, Theorem 2.4.3 and Corrolary 2.4.4]. This is confirmed by our numerical tests, see the convergence curves for this case in Figure 13. The linear behavior for small h could be caused by the fact that the reference solution p_η^* might not be computed on a fine enough grid.

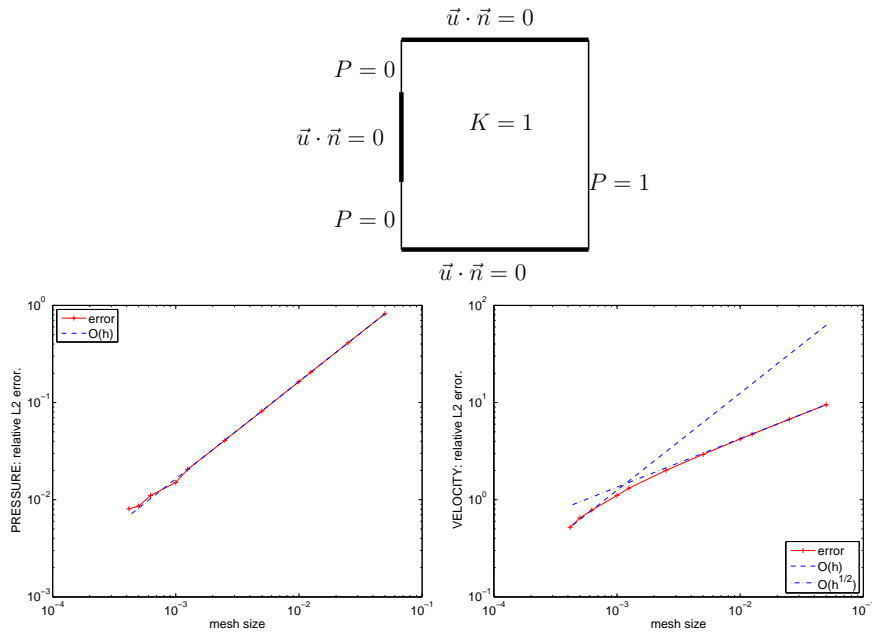


Figure 13: Problem with less regularity: Neumann and Dirichlet boundary conditions on the lefthand side. Top: description of the problem. Bottom left: convergence history in the L^2 norm of the pressure ($\mathcal{O}(h)$). Bottom right: idem for the velocity ($\mathcal{O}(h^{1/2})$). Compare with Figures 12.

Finally, in Figure 14, we show what happens when there is no fracture above and below the barrier (when $y < 1/4$ or $y > 3/4$). Instead, the continuity of p_h and $\mathbf{u}_h \cdot \mathbf{n}$ between Ω_1 and Ω_2 is weakly imposed using the mortar method, [5]. A fine mesh was used for the fracture as well as for the mortars above and below the fracture. As is well known, the mortar space cannot be too rich, otherwise convergence or even solvability can be jeopardized. We clearly notice large oscillations that do not decrease with h , in the mortar zone, in contrast to what occurs when there is a fracture with the same properties as the surrounding rock, see Figure 11.

4.5 Third test-case : a mixed fracture (highly permeable/barrier)

In this third test-case (see Figure 3), the permeability K_f in the fracture is $K_f = 2000$ at the extremities, yielding $K_\gamma = K_f d = 2$, and $K_f = 1/2000$ in the central half of the fracture, thus yielding there $\kappa_\gamma = 2K_f/d = 1$. Dirichlet

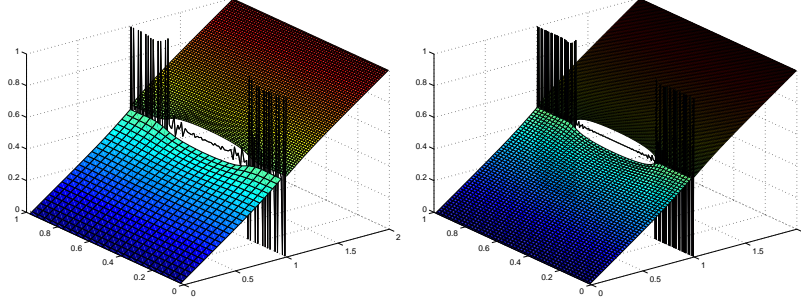


Figure 14: Barrier in the central zone, and mortar elements outside (no fracture). Pressure evolution when h is refined (**fine** fracture case). Left: $h_1 = 1/24, h_\gamma = 1/128, h_2 = 1/64$. Right: $h_1 = 1/48, h_\gamma = 1/256, h_2 = 1/128$. $K_f = 0.002, d = 0.001$. While the oscillations in the fracture decrease with h (center), the mortar oscillations do not. Compare with Figure 11.

conditions are imposed on the fracture boundaries: there is a unit pressure drop from the top of the fracture to the bottom. Thus the fluid tends to flow from right to left, and also flows rapidly along the very permeable part of the fracture from top to bottom, but avoids the central zone. There is fluid exchange between the fracture and the rock matrix as fluid from the fracture enters the rock matrix at the top and fluid from the matrix enters the fracture at the bottom. The normal velocity is discontinuous across the permeable part of the fracture and the pressure is discontinuous in the central zone.

A reference computation performed with a conforming mesh is shown in Figure 15.

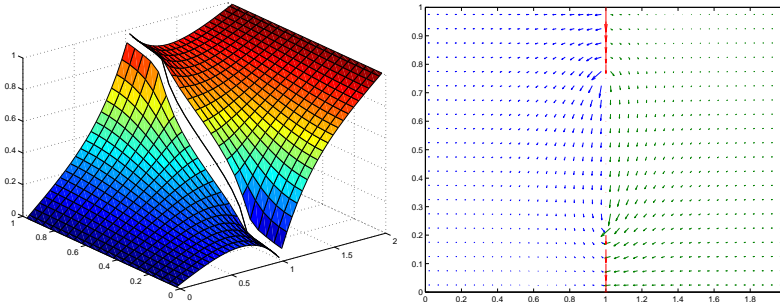


Figure 15: Test case 3. Pressure (left) and Darcy velocity (right) with conforming meshes ($h_1 = h_2 = h_\gamma = 1/20$). $K_f = 2000$ (top and bottom of the fracture) and $K_f = 1/2000$ (central part), $d = 0.001$.

A solution obtained with a nonconforming mesh is shown in Figure 16 in the case of a refined fracture mesh, and in Figure 17 in the case of a coarse fracture mesh. One notices again large spurious pressure oscillations in the low permeability zone, that decrease when refining while keeping the same relation between h_1, h_2 and h_γ : see Figure 18. We also report the behavior of the pressure as h decreases in Figure 19 in the case in which h_γ is refined where

the permeability K_f is large, and is coarse where K_f is low. The spurious oscillations are damped more rapidly in this case.

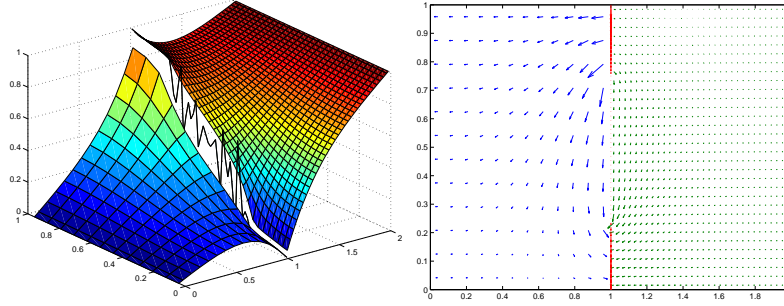


Figure 16: Test case 3. Pressure (left) and Darcy velocity (right) with non-conforming meshes: $h_1 = 1/12, h_\gamma = 1/64, h_2 = 1/32$ (the fracture mesh is **finer** than the other meshes). $K_f = 2000$ and $K_f = 1/2000, d = 0.001$.

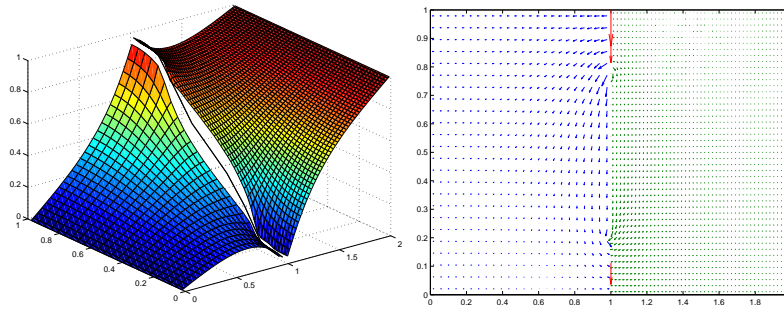


Figure 17: Test case 3. Pressure (left) and Darcy velocity (right) with non-conforming meshes: $h_1 = 1/24, h_\gamma = 1/9, h_2 = 1/47$ (the fracture mesh is **coarser** than the other meshes). $K_f = 2000$ and $K_f = 1/2000, d = 0.001$.

In Figure 20, the L^2 norm convergence curves for the pressure and for the Darcy velocity are shown for a discretization with a finely meshed fracture and with a coarsely meshed fracture. As before for comparison, we also show the convergence with conforming meshes, which is very similar to that of the finely mesh case. The convergence for both pressure and velocity is linear as expected.

4.6 Conclusions concerning the numerical simulations

As expected theoretically, the L^2 convergence for the pressure is $\mathcal{O}(h)$ in all cases. The convergence of the velocity is also in good agreement with the theory, although in some cases, due to a lack of regularity of the solution, we do not obtain $\mathcal{O}(h)$ behavior.

From the limited numerical experiments shown here, the following conclusions can be drawn: when the fracture is very permeable, one should refine the fracture mesh more than the mesh in the surrounding rock, as this both avoids small oscillations and improves the precision at the very location where the fluid

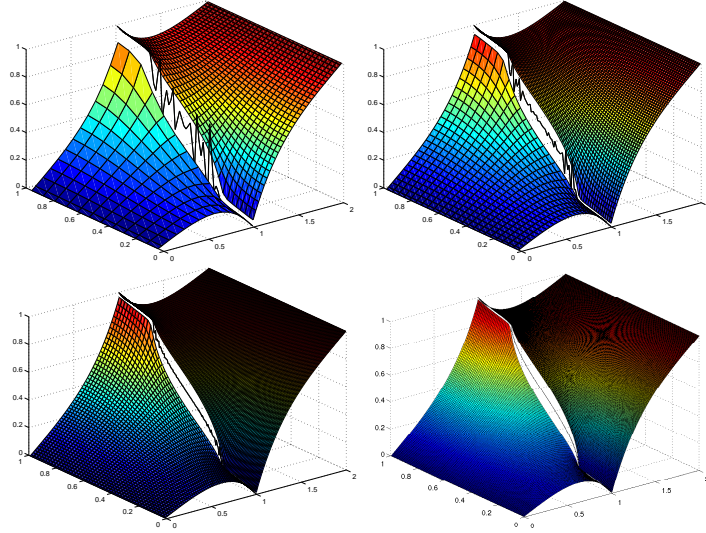


Figure 18: Test case 3. Pressure evolution when h is refined (**fine** fracture case). $h_1 = 1/(12n)$, $h_\gamma = 1/(64n)$, $h_2 = 1/(32n)$ and $n = 1, 2, 4, 8$ (top left, top right, bottom left, bottom right). $K_f = 20000$ and $K_f = 1/20000$, $d = 0.001$. The oscillations decrease with h .

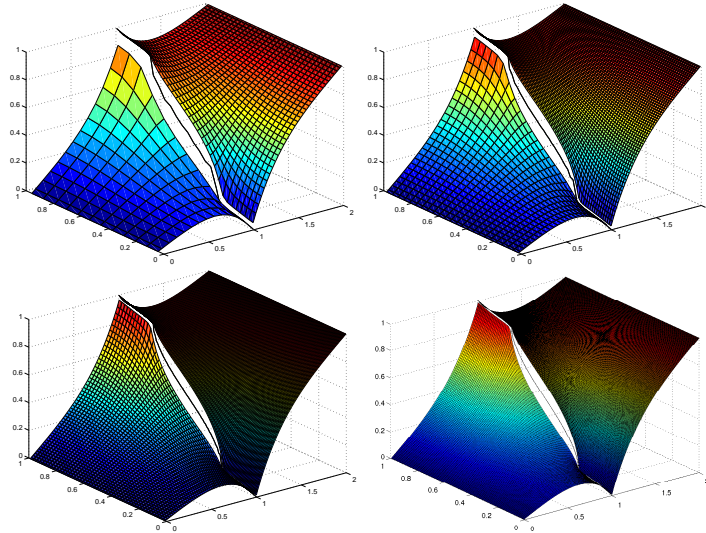


Figure 19: Test case 3. Pressure evolution when h is refined (**fine** fracture case). $h_1 = 1/(12n)$, $h_2 = 1/(32n)$ and $n = 1, 2, 4, 8$ (top left, top right, bottom left, bottom right). This time, h_γ is not constant: it is coarser in the middle of the fracture: $h_{\gamma, mid} \approx 1/(25n)$ and $h_{\gamma, top/bot} \approx 1/(100n)$. We use the same number of fracture cells as in Figure 18. $K_f = 0.002$ and $K_f = 1/2000$, $d = 0.001$. The oscillations decrease more rapidly with h than in Figure 18.

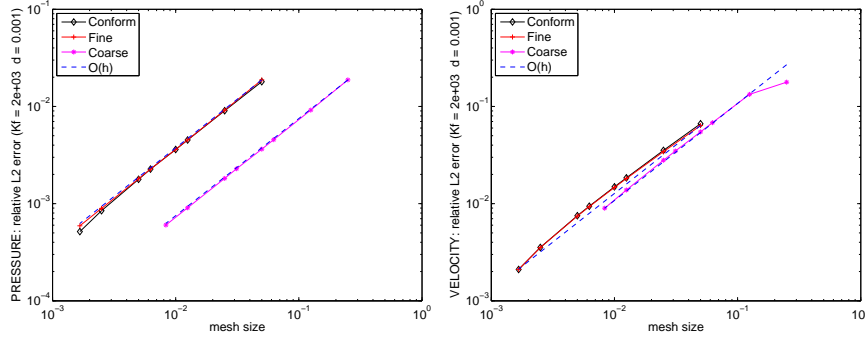


Figure 20: Test case 3. Discrete relative L^2 error as a function of h . The three meshes are nonconforming at the interface, and the fracture is either **finely** (crosses) or **coarsely** (stars) meshed. $h_1 \approx h_2 \in [1/20, 1/600]$, and $h_\gamma \approx 0.1 h_1$ (finely meshed fracture) or $h_\gamma \approx 5 h_1$ (coarsely meshed fracture). $K_f = 2000$ and $K_f = 1/2000$, $d = 0.001$. **Left:** pressure error. **Right:** velocity error.

flows most rapidly. When the fracture is a barrier, one should on the contrary use a rather coarse fracture mesh, as this avoids troublesome, possibly large oscillations in the pressure and further there is no need to have a fine discretization in a zone where almost no fluid flows. It might be useful, however, to refine at the tips of the fracture, but this has not been investigated here.

5 Conclusion

In this article, we analyze, both theoretically and with numerical experiments, the effect of nonconformity of the mesh on a model for flow in a porous medium with a fracture. Contrary to what is seen when no equations are solved on the interface, as in the mortar methods [5], the fracture equations result in a “stabilizing” effect that allows for an arbitrary meshing of the fracture.

References

- [1] C. Alboin, J. Jaffré, J. E. Roberts, and C. Serres. Modeling fractures as interfaces for flow and transport in porous media. In Zhangxin Chen and Richard E. Ewing, editors, *Fluid flow and transport in porous media: mathematical and numerical treatment (South Hadley, MA, 2001)*, number 295 in Contemp. Math., pages 13–24, Providence, RI USA, 2002. Amer. Math. Soc.
- [2] C. Alboin, J. Jaffré, J.E. Roberts, and C. Serres. Domain decomposition for flow in porous fractured media. In C.-H. Lai, P. E. Bjorstad, M. Cross, and O. B. Widlund, editors, *Domain Decomposition Methods in Sciences and Engineering*, Domain Decomposition Methods in Sciences and Engineering, pages 365–373. Domain Decomposition Press, 1999.
- [3] L. Amir, M. Kern, V. Martin, and J. E. Roberts. Décomposition de domaine pour un milieu poreux fracturé : un modèle en 3d avec fractures qui s’intersectent. *ARIMA*, 5:11–25, 2006.
- [4] Ph. Angot, F. Boyer, and F. Hubert. Asymptotic and numerical modelling of flows in fractured porous media. *M2AN*, 43(2):239–275, 2009.
- [5] T. Arbogast, L. C. Cowsar, M. F. Wheeler, and I. Yotov. Mixed finite element methods on non-matching multiblock grids. *SIAM J. Numer. Anal.*, 37:1295–1315, 2000.
- [6] C. Bernardi, Y. Maday, and A. T. Patera. A new nonconforming approach to domain decomposition: the mortar element method. In *Nonlinear partial differential equations and their applications. Collège de France Seminar, Vol. XI (Paris, 1989–1991)*, volume 299 of *Pitman Res. Notes Math. Ser.*, pages 13–51. Longman Sci. Tech., Harlow, 1994.
- [7] F. Brezzi and M. Fortin. *Mixed and Hybrid Finite Element Methods*. Springer-Verlag, Berlin, New York, 1991.
- [8] C. D’Angelo and A. Scotti. A mixed finite element method for Darcy flow in fractured porous media with non-matching grids. *Submitted*, 2010.
- [9] N. Frih, J. E. Roberts, and A. Saada. Un modèle Darcy-Forchheimer pour un écoulement dans un milieu poreux fracturé. *ARIMA*, 5:129–143, 2006.
- [10] N. Frih, J. E. Roberts, and A. Saada. Modeling fractures as interfaces: a model for Forchheimer fractures. *Comput. Geosci.*, 12:91–104, 2008.
- [11] P. Grisvard. *Singularities in boundary value problems*, volume 22 of *Recherches en Mathématiques Appliquées [Research in Applied Mathematics]*. Masson, Paris, 1992.
- [12] P. Knabner and J. E. Roberts. Coupling Forchheimer flow in fractures with Darcy flow in the rock matrix. *submitted*, 2011.
- [13] V. Martin, J. Jaffré, and J. E. Roberts. Modeling fractures and barriers as interfaces for flow in porous media. *SIAM J. Sci. Comput.*, 26(5):1667–1691, 2005.

- [14] F. Moreles and R. E. Showalter. The narrow fracture approximation by channeled flow. *JMAA*, 365(1):320–331, 2010.
- [15] V. Reichenberger, H. Jakobs, P. Bastian, and R. Helmig. A mixed-dimensional finite volume method for multiphase flow in fractured porous media. *Adv. Water Resources*, 29(7):1020–1036, 2006.
- [16] J. E. Roberts and J.-M. Thomas. Mixed and hybrid methods. In P. G. Ciarlet and J.-L. Lyons, editors, *Handbook of Numerical Analysis*, volume 2, pages 523–639. Elsevier, Amsterdam, New York, 1991.

Contents

1	Introduction	3
2	Description of the problem	3
3	Weak formulation of the model problem	5
4	Discretization	6
4.1	Interpolation estimates	7
4.2	Approximation estimates	9
4.3	First test-case : a highly permeable fracture	13
4.4	Second test-case: a geological barrier	16
4.5	Third test-case : a mixed fracture (highly permeable/barrier) . .	19
4.6	Conclusions concerning the numerical simulations	21
5	Conclusion	23



Centre de recherche INRIA Paris – Rocquencourt
Domaine de Voluceau - Rocquencourt - BP 105 - 78153 Le Chesnay Cedex (France)

Centre de recherche INRIA Bordeaux – Sud Ouest : Domaine Universitaire - 351, cours de la Libération - 33405 Talence Cedex
Centre de recherche INRIA Grenoble – Rhône-Alpes : 655, avenue de l'Europe - 38334 Montbonnot Saint-Ismier
Centre de recherche INRIA Lille – Nord Europe : Parc Scientifique de la Haute Borne - 40, avenue Halley - 59650 Villeneuve d'Ascq
Centre de recherche INRIA Nancy – Grand Est : LORIA, Technopôle de Nancy-Brabois - Campus scientifique
615, rue du Jardin Botanique - BP 101 - 54602 Villers-lès-Nancy Cedex
Centre de recherche INRIA Rennes – Bretagne Atlantique : IRISA, Campus universitaire de Beaulieu - 35042 Rennes Cedex
Centre de recherche INRIA Saclay – Île-de-France : Parc Orsay Université - ZAC des Vignes : 4, rue Jacques Monod - 91893 Orsay Cedex
Centre de recherche INRIA Sophia Antipolis – Méditerranée : 2004, route des Lucioles - BP 93 - 06902 Sophia Antipolis Cedex

Éditeur
INRIA - Domaine de Voluceau - Rocquencourt, BP 105 - 78153 Le Chesnay Cedex (France)
<http://www.inria.fr>
ISSN 0249-6399